

# Fano resonances in a single defect nanocavity coupled with a plasmonic waveguide

Jianjun Chen,<sup>1,2</sup> Chengwei Sun,<sup>1,2</sup> and Qihuang Gong<sup>1,2,\*</sup>

<sup>1</sup>State Key Laboratory for Mesoscopic Physics and Department of Physics, Peking University, Beijing 100871, China

<sup>2</sup>Collaborative Innovation Center of Quantum Matter, Beijing, China

\*Corresponding author: qhgong@pku.edu.cn

Received September 30, 2013; revised November 20, 2013; accepted November 22, 2013;  
posted November 22, 2013 (Doc. ID 198582); published December 19, 2013

Two Fano resonances are theoretically predicted in a single defect nanocavity, consisting of a rectangular cavity with a small stub defect, side-coupled with a plasmonic waveguide. These two Fano resonances are found to originate from two different mechanisms. One is caused by the excitation of a high-order resonant mode in the rectangular cavity owing to the structural breaking, and the other is attributed to the inherent resonant mode in the small stub defect. The narrow high-order mode and inherent mode couple with the broad low-order resonant mode in the rectangular cavity, giving rise to two Fano resonances. Because of the different origins, these two Fano resonances exhibit quite different responses to the variations of the structural dimensions. This has important applications in highly sensitive and multiparameter sensing in the complicated environments. © 2013 Optical Society of America

OCIS codes: (240.6680) Surface plasmons; (260.3160) Interference; (280.4788) Optical sensing and sensors.

<http://dx.doi.org/10.1364/OL.39.000052>

Fano resonances in metallic nanostructures are a coupling effect which results from the interaction of a narrow dark resonant mode with a broad bright one [1–3]. Different from Lorentzian resonances supported by the universal resonators, Fano resonances exhibit sharp and asymmetric spectral line shapes together with strong field enhancements. These properties show potential applications in the areas of nonlinearities, lasing, biosensors, and modulators [1–4]. Thus, tremendous attention was attracted to designing various metallic structures to obtain Fano resonances in the past decade. For example, the plasmonic array structures ranging from particle lattices and oligomers to nanowire lattices and splitting-type structures [5–18] were proposed to realize Fano resonances. For highly integrated photonic circuits, these array structures [5–18] are a little bulky and complicated. This makes them difficult to integrate into chips. Recently, using waveguide-cavity structures, which consist of a plasmonic waveguide coupled with two or more cavities of comparative dimensions, Fano resonances were also theoretically predicted [19–27] and even experimentally demonstrated [4,28]. Compared with array structures, plasmonic waveguide-cavity structures are much compact and simple. This miniaturization together with planar waveguide configurations make waveguide-cavity structures easy to integrate into chips. Note that all of the Fano resonances in the plasmonic waveguide-cavity structures [4,19–28] were based on the coupled-resonator effect, involving various cavities with comparative dimensions.

In the Letter, two Fano resonances based on two different physical mechanisms are theoretically predicted in a single defect nanocavity, comprised of a rectangular cavity with a small stub defect. Simulations find that one Fano resonance results from the excitation of a high-order resonant mode in the rectangular cavity because of the structural breaking [1,2,5], and the other is attributed to the inherent resonant mode in the small stub. These two resonant modes exhibit narrowband response spectra, compared with that in the broad Lorentzian resonant mode (low-order mode) which usually emerges in

a rectangular cavity. As a result, the coupling between the narrow resonant modes and the broad Lorentzian resonant mode gives rise to two Fano resonances. Obviously, the physical mechanisms of the two Fano resonances differ from the coupled-resonator effect in the plasmonic waveguide-cavity structures with various cavities [4,19–28]. Additionally, it is found that these two Fano resonances have quite different responses to the variations of the structural dimensions because of their different physical origins. This may be of importance in achieving highly sensitive and accurate sensing in complicated environments. It also may reveal important applications in multiparameter sensing.

The proposed single defect nanocavity is schematically shown in Fig. 1, which consists of a rectangular cavity with a small stub on one edge. This defect cavity is side-coupled with a metal-insulator-metal (MIM) waveguide, which can support surface-plasmon-polariton (SPP) modes [21–23,29]. This system is a two-dimensional model, and the gray and white parts in Fig. 1 denote Ag and air, respectively. The length and height of the rectangular cavity are  $L$  and  $H$ , respectively. The depth and width of the small stub defect are  $d$  and  $w$  ( $w \ll L$ ), respectively. In the plasmonic cavity, the accumulated phase shift per round trip for the SPPs is  $\Phi = 4\pi \times n_{\text{eff}} \times L/\lambda + 2\varphi$  [28–30]. Constructive interference should occur when  $\Phi$  equals  $2m\pi$ , and thus the resonant wavelength is determined by

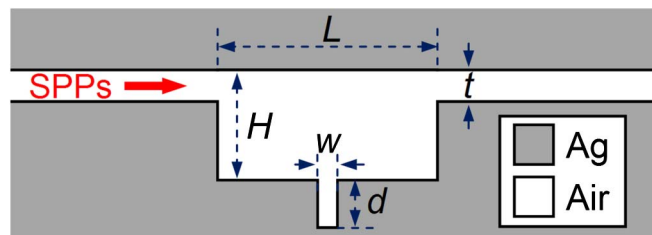


Fig. 1. Schematic and geometrical parameters of the defect nanocavity side-coupled with a MIM waveguide.

$$\lambda = 2n_{\text{eff}}L/(m - \varphi/\pi), \quad (1)$$

where  $n_{\text{eff}}$  represents the effective refractive index of the SPPs,  $\varphi$  is the phase shift brought by the SPP reflection off the metal wall in the cavity, and  $m$  is the resonant order. Based on Eq. (1), the resonant wavelength of  $\lambda$  is proportional to the cavity length of  $L$ , and the proportionality coefficient is

$$d\lambda/dL = 2n_{\text{eff}}/(m - \varphi/\pi). \quad (2)$$

In order to investigate the optical responses of the defect nanocavity, its transmission spectra are simulated by using the finite element method (FEM) of Comsol Multiphysics. In the simulations, the MIM dielectric gap is assumed to be  $t = 50$  nm and is fixed throughout this Letter. The transmittance of the SPPs in the MIM waveguide structure is defined as the quotient between the SPP power flows (obtained by integrating the Poynting vector over the cross section of the MIM waveguide) of an observing port with and without the rectangular cavity [23,26]. The transmission spectra of the single defect cavity are obtained by changing the input wavelength of  $\lambda$ . The permittivity of Ag as a function of  $\lambda$  is taken from the experiment results [31] and expanded by using the method of interpolation (1 nm).

First, we fix the dimensions of the small stub to be  $w = 20$  nm and  $d = 100$  nm, and then calculate the transmission spectra of the defect nanocavity by varying the cavity length of  $L$ . The calculated transmission spectra are displayed in Figs. 2(a)–2(f), where the cavity height is set to be  $H = 275$  nm. Obviously, two Fano resonances together with a broad Lorentzian resonant mode are observed in each of the transmission spectra. The left Fano resonance (denoted by FL) and the broad Lorentzian resonant mode are linearly redshifted with increasing cavity length, as shown by the purple dotted line and the blue

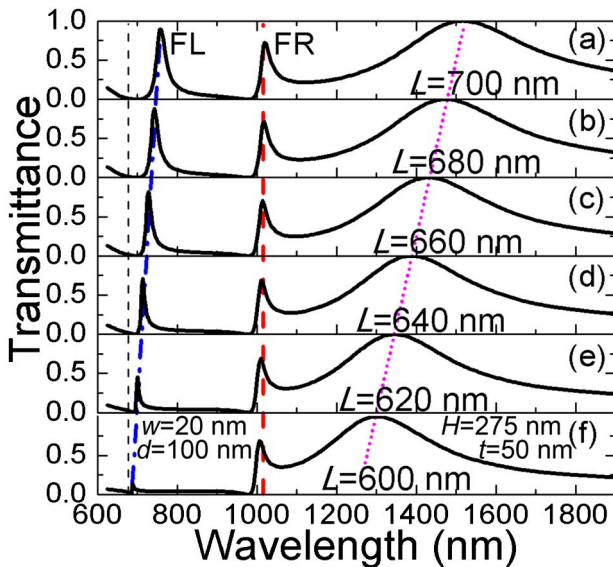


Fig. 2. Transmission spectra of the defect nanocavity for different cavity lengths of (a)  $L = 700$  nm, (b)  $L = 680$  nm, (c)  $L = 660$  nm, (d)  $L = 640$  nm, (e)  $L = 620$  nm, and (f)  $L = 600$  nm when the dimension of the small stub defect is fixed to be  $w = 20$  nm and  $d = 100$  nm.

dashed-dotted line in Fig. 2, respectively. However, the position of the right Fano resonance (denoted by FR) nearly remains unchanged, as depicted by the red dashed line in Fig. 2. This indicates that these two Fano resonances may come from different mechanisms. In order to understand the underlying physics of the transmission spectra in the defect nanocavity, these three resonant modes are investigated one by one in the following.

For simplicity, we begin with the broad Lorentzian resonant mode, which exhibits a broadband transmission spectrum with a nearly symmetric Lorentzian-like profile, as shown in Fig. 2. The field distribution in the defect cavity at the resonant wavelength (transmission peak) for this mode is displayed in Fig. 3(a), revealing a two-order resonant mode (two antinodes in the standing wave pattern) in the rectangular cavity. Thus, the Lorentzian resonant mode is supported in the rectangular cavity, and its resonant wavelength is linearly redshifted with increasing cavity length of  $L$ , as shown by the purple dotted line (with a slope of  $\Delta\lambda/\Delta L \approx 2$ ) in Fig. 2. This linear dependence between the resonant wavelength and the cavity length agrees well with the results in literatures [29,30], as well as Eq. (2). In particular, it is observed that the antinodes of the standing wave pattern appear on both the left and right edges of the cavity, as shown in Fig. 3(a). Hence, the power flow of this mode in the rectangular cavity can be easily leaked and coupled into the MIM waveguide that connects the rectangular cavity. This leak of power flow is a large loss for the rectangular cavity. As a result, the Lorentzian resonant mode exhibits a broadband transmission spectrum with a bandwidth of about  $\Delta\lambda_{\text{FWHM}} \approx 450$  nm, as shown in Fig. 2.

For the left Fano resonance (FL), it is also redshifted when the cavity length increases, as shown by the blue dashed-dotted line (with a slope of  $\Delta\lambda/\Delta L \approx 1$ ) in Fig. 2. The field distribution at the resonant wavelength (transmission peak) of this Fano resonance is displayed in Fig. 3(b). Evidently, a standing wave pattern with strong intensities is excited in the rectangular nanocavity because of the structural breaking [1,2,5]. There are three antinodes in the standing wave pattern, revealing that a high-order resonant mode (three-order oscillation) is excited in the rectangular cavity. For this high-order resonant mode, at the connection part between the MIM waveguide and the cavity is a node, as shown in Fig. 3(b). This makes the power flow of the mode in the rectangular cavity difficult to be leaked into the MIM waveguide, and thus the power of the mode is well trapped in the rectangular cavity, as shown in Fig. 3(b). Hence, this high-order

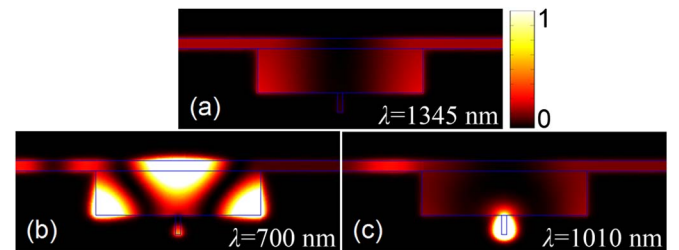


Fig. 3. Field distributions ( $|H_z|^2$ ) for the cavity length of  $L = 620$  nm at the resonant wavelengths of (a)  $\lambda = 1345$  nm, (b)  $\lambda = 700$  nm, and (c)  $\lambda = 1010$  nm. Here,  $H_z$  represents the magnetic field.

resonant mode is a strong trapped mode with a narrow-band response spectrum. Just like the broad Lorentzian resonant mode, the resonant wavelength of the high-order mode would linearly redshift with an increase in cavity length of  $L$  ( $\Delta\lambda/\Delta L \approx 1$ ). Obviously, this redshift for the three-order mode becomes slower than that for the broad Lorentzian resonant mode ( $\Delta\lambda/\Delta L \approx 2$ ). The main reason is that  $m$  becomes large for the high-order resonant mode [see Eq. (2)]. Based on Eq. (2), it is easy to get that  $d\lambda/dL \approx 2 \times 1/(2 - \pi/\pi) = 2$  for the broad low-order resonant mode. For the high-order resonant mode, the round trip is: the bottom left corner  $\rightarrow$  the top metal wall  $\rightarrow$  the bottom right corner  $\rightarrow$  the bottom left corner. This special oscillation trip is attributed to the structural break in the defect nanocavity. Herein, the effective cavity length becomes  $L \times [1 + 1/\cos(\text{atan}(2H/L))]/2 \approx 1.1L$ . Hence, Eq. (2) becomes  $d\lambda/dL \approx 2 \times 1/(3 - \pi/\pi) \times [1 + 1/\cos(\text{atan}(2H/L))]/2 \approx 1$  for the high-order resonant mode. These results agree well with the slopes of the purple dashed line and the blue dashed-dotted line in Fig. 2. In the rectangular cavity, the narrow high-order resonant mode will interfere with the broad low-order resonant mode, resulting in a Fano resonance, as shown in Fig. 2. Therefore, the position of this Fano resonance is redshifted as the cavity length increases.

For the right Fano resonance (FR), it is observed that its position hardly varies when increasing the cavity length, as displayed by the red dashed line in Fig. 2. The field distribution at the resonant wavelength (transmission peak) of the right Fano resonance is displayed in Fig. 3(c). It is evident that a strong field distribution is observed in the small stub defect (one antinode in the standing wave pattern). This reveals that the small stub defect supports a strong resonant mode (one-order oscillation) with a narrowband response spectrum [1]. This resonant mode is an inherent mode in the small stub defect, and its resonant wavelength is determined by the stub dimension [21,26,29,30]. This narrow inherent mode in the small stub defect couples with the broad Lorentzian mode in the rectangular cavity, giving rise to the right Fano resonance. Therefore, the variation of the cavity length nearly has no influence on the position of the right Fano resonance when the stub dimension is fixed, as shown by the red dashed line in Fig. 2.

To further test our analysis, the transmission spectra of the defect cavity are calculated by varying the dimensions of the small stub defect (e.g., the depth of  $d$ ), and the results are displayed in Fig. 4. In this case, the rectangular cavity dimensions are fixed to be  $L = 620$  nm and  $H = 275$  nm. It is observed that the broad low-order resonant mode in the rectangular cavity and the left Fano resonance are hardly varied because their resonant wavelengths are determined by the fixed values of  $L$  and  $H$  in the rectangular cavity [29,30], as shown by the purple dotted and blue dashed-dotted lines in Fig. 4. However, the situation becomes quite different for the right Fano resonance. Increasing  $d$  can greatly redshift the resonant wavelength of the inherent resonant mode in the small stub defect [21,26,29,30]. Hence, the right Fano resonance, resulting from the coupling between the inherent resonant mode in the small stub defect and the broad low-order resonant mode in the rectangular cavity, is linearly redshifted largely when the depth of

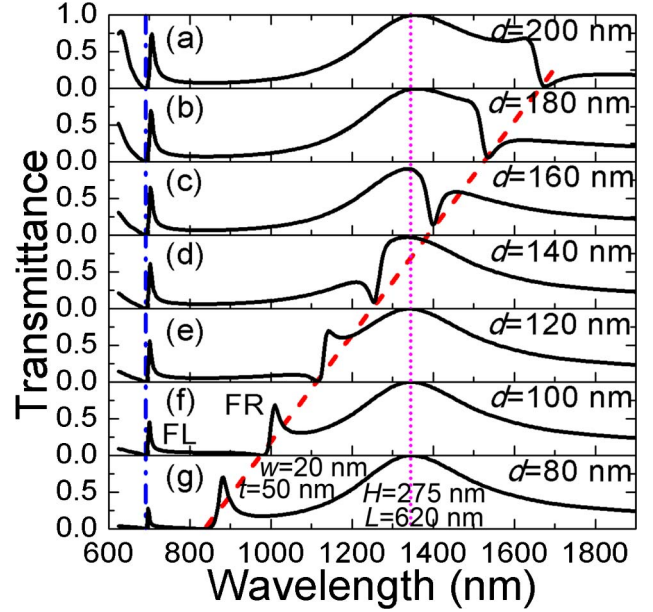


Fig. 4. Transmission spectra for different small stub depths of (a)  $d = 200$  nm, (b)  $d = 180$  nm, (c)  $d = 160$  nm, (d)  $d = 140$  nm, (e)  $d = 120$  nm, (f)  $d = 100$  nm, and (g)  $d = 80$  nm when the dimension of the rectangular cavity is fixed to be  $L = 620$  nm and  $H = 275$  nm.

the small stub defect increases, as shown by the red dashed line (with a slope of  $\Delta\lambda/\Delta d \approx 7$ ) in Fig. 4. The large wavelength shift with varying  $d$  is because the order of the inherent resonance is low ( $m = 1$ ) and the effective refractive index of the SPP waveguide mode becomes large ( $n_{\text{eff}} \approx 1.8$ ) in the stub defect [20,25,28,29]. In the stub defect, there is only one reflection off the metal wall, and thus the proportionality coefficient is changed to  $d\lambda/d(d) = 2n_{\text{eff}}/[m - \varphi/(2\pi)] = 2 \times 1.8/[1 - \pi/(2\pi)] \approx 7$ , agreeing well with the slope of the red dashed line in Fig. 4. Note that the dependencies of these two Fano resonances on the structural dimensions coincide with the above analysis very well. Therefore, it can be concluded that these two Fano resonances in the defect cavity result from the high-order resonant mode in the rectangular cavity and the inherent resonant mode in the small stub defect, respectively. These different origins make the two Fano resonances exhibit quite different responses to the variations of the structural dimensions, as shown in Figs. 2 and 4.

For the Fano resonances in the defect nanocavity, the transmittance of the SPPs varies sharply from the valley to the peak with only a significantly decreased wavelength shift ( $\Delta\lambda \approx 4$  nm), which is much smaller than that in the broad low-order resonant case ( $\Delta\lambda_{\text{FWHM}} \approx 450$  nm) [see Fig. 4(g)]. This reveals that the wavelength shift required for a completely on/off variation is significantly reduced, implying a high sensitivity to the index variations of a nearby or surrounding medium [2,4,28]. These pronounced properties in the single defect nanocavity, such as the small required wavelength shifts, the strong field enhancements, and the increased sensitivity to the index variations, can be used in the applications of sensing [2,4,28]. More importantly, since these two Fano resonances originate from different mechanisms and have



quite different responses to the variations of the structural parameters, the defect nanocavity can be exploited to develop more functional and complex devices. For example, when a detected sample (e.g., gas, liquid, or biomolecule) is only filled in the rectangular cavity, the left Fano resonance would have a corresponding wavelength shift [4,29] with a sensitivity of about 700 nm/RIU, (588 nm/RIU in [12]), while the right Fano resonance remains unchanged. Usually, for a high-sensitivity sensor, the environment elements, such as the temperature fluctuation, can also shift the resonant wavelength and thus affect the measurement results [32,33]. Luckily, in the defect nanocavity, the right Fano resonance can also be shifted by the environment elements. This shift of the right Fano resonance can be used to monitor the environment elements. This can remove the influence brought by the environment elements to get accurate measurements. The utilization of two Fano resonances resulting from different mechanisms in the single defect nanocavity may lead to important applications in realizing highly sensitive and accurate sensing in complicated environments, as well as multiparameter sensing.

In summary, two Fano resonances were theoretically predicted in a single defect nanocavity, comprised of a rectangular cavity with a small stub side-coupled with a plasmonic waveguide. Simulations found that the high-order resonant mode excited in the defect cavity and the inherent resonant mode in the small stub were responsible for these two Fano resonances, respectively. This is different from the coupled-resonator effect in the previous waveguide-cavity structures [4,19–28] with various cavities. These two Fano resonances resulted from different mechanisms and thus had different responses to the variations of the structural dimensions. This made it have more functional and complex applications. This also may pave new routes to realizing Fano resonances in on-chip plasmonic nanostructures.

This work was supported by the National Basic Research Program of China (Grant No. 2013CB328704) and the National Natural Science Foundation of China (Grant Nos. 11204018 and 11134001).

## References

1. A. E. Miroshnichenko, S. Flach, and Y. S. Kivshar, *Rev. Mod. Phys.* **82**, 2257 (2010).
2. B. Luk'yanchuk, N. I. Zheludev, S. A. Maier, N. J. Halas, P. Nordlander, H. Giessen, and C. T. Chong, *Nat. Mater.* **9**, 707 (2010).
3. B. Gallinet and O. J. F. Martin, *ACS Nano* **5**, 8999 (2011).
4. J. Chen, Z. Li, X. Zhang, J. Xiao, and Q. Gong, *Sci. Rep.* **3**, 1451 (2013).
5. V. A. Fedotov, M. Rose, S. L. Prosvirnin, N. Papasimakis, and N. I. Zheludev, *Phys. Rev. Lett.* **99**, 147401 (2007).
6. A. Christ, O. J. F. Martin, Y. Ekinici, N. A. Gippius, and S. G. Tikhodeev, *Nano Lett.* **8**, 2171 (2008).
7. A. Christ, Y. Ekinici, H. H. Solak, N. A. Gippius, S. G. Tikhodeev, and O. J. F. Martin, *Phys. Rev. B* **76**, 201405 (2007).
8. Z. K. Zhou, X. N. Peng, Z. J. Yang, Z. S. Zhang, M. Li, X. R. Su, Q. Zhang, X. Y. Shan, Q. Q. Wang, and Z. Y. Zhang, *Nano Lett.* **11**, 49 (2011).
9. N. Liu, L. Langguth, T. Weiss, J. Kastel, M. Fleischhauer, T. Pfau, and H. Giessen, *Nat. Mater.* **8**, 758 (2009).
10. S. Zhang, D. A. Genov, Y. Wang, M. Liu, and X. Zhang, *Phys. Rev. Lett.* **101**, 047401 (2008).
11. M. Hentschel, M. Saliba, R. Vogelgesang, H. Giessen, A. P. Alivisatos, and N. Liu, *Nano Lett.* **10**, 2721 (2010).
12. N. Liu, T. Weiss, M. Mesch, L. Langguth, U. Eigenthaler, M. Hirscher, C. Sonnichsen, and H. Giessen, *Nano Lett.* **10**, 1103 (2010).
13. K. Aydin, I. M. Pryce, and H. A. Atwater, *Opt. Express* **18**, 13407 (2010).
14. A. Artar, A. A. Yanik, and H. Altug, *Nano Lett.* **11**, 1685 (2011).
15. M. Hentschel, D. Dregely, R. Vogelgesang, H. Giessen, and N. Liu, *ACS Nano* **5**, 2042 (2011).
16. M. Rahmani, B. Lukiyanchuk, B. Ng, A. Tavakkoli, Y. F. Liew, and M. H. Hong, *Opt. Express* **19**, 4949 (2011).
17. J. Zhang, W. L. Bai, L. K. Cai, Y. Xu, G. F. Song, and Q. Q. Gan, *Appl. Phys. Lett.* **99**, 181120 (2011).
18. I. Baryakhtar, Y. Demidenko, and V. Lozovski, *J. Opt. Soc. Am. B* **30**, 1022 (2013).
19. R. D. Kekatpure, E. S. Barnard, W. S. Cai, and M. L. Brongersma, *Phys. Rev. Lett.* **104**, 243902 (2010).
20. Y. R. He, H. Zhou, Y. Jin, and S. L. He, *Appl. Phys. Lett.* **99**, 043113 (2011).
21. J. J. Chen, Z. Li, J. Li, and Q. H. Gong, *Opt. Express* **19**, 9976 (2011).
22. Z. H. Han and S. I. Bozhevolnyi, *Opt. Express* **19**, 3251 (2011).
23. J. J. Chen, Z. Li, M. Lei, X. L. Fu, J. H. Xiao, and Q. H. Gong, *Plasmonics* **7**, 441 (2012).
24. X. Piao, S. Yu, and N. Park, *Opt. Express* **20**, 18994 (2012).
25. H. Lu, X. M. Liu, D. Mao, Y. K. Gong, and G. X. Wang, *Opt. Lett.* **36**, 3233 (2011).
26. J. Chen, C. Wang, R. Zhang, and J. Xiao, *Opt. Lett.* **37**, 5133 (2012).
27. G. X. Wang, H. Lu, and X. M. Liu, *Opt. Express* **20**, 20902 (2012).
28. J. Chen, Z. Li, S. Yue, J. Xiao, and Q. Gong, *Nano Lett.* **12**, 2494 (2012).
29. F. Hu, H. Yi, and Z. Zhou, *Opt. Lett.* **36**, 1500 (2011).
30. Q. Zhang, X. Huang, X. Lin, J. Tao, and X. Jin, *Opt. Express* **17**, 7549 (2009).
31. P. B. Johnson and R. W. Christy, *Phys. Rev. B* **6**, 4370 (1972).
32. J. G. Zhu, S. K. Ozdemir, Y. F. Xiao, L. Li, L. N. He, D. R. Chen, and L. Yang, *Nat. Photonics* **4**, 46 (2009).
33. L. B. Shao, X. F. Jiang, X. C. Yu, B. B. Li, W. R. Clements, F. Vollmer, W. Wang, Y. F. Xiao, and Q. H. Gong, *Adv. Mater.* **25**, 5616 (2013).